Chemistry Africa (2022) 5:589–606
https://doi.org/10.1007/s42250-022-00343-2

ORIGINAL ARTICLE

Preparation of Magnesium Doped Magnetic Nanoferrite and its Clay-Based composite: Application to the Removal of an Anionic Dye from Wastewater

Sabrine Saad[1] · Sarra Ben Amor[1] · Amel Ben Slimane[1]

Received: 24 February 2022 / Accepted: 3 March 2022 / Published online: 22 March 2022

Abstract

Magnetic ferrite (Mg-doped bismuth ferrite) and its clay-based composite (Mg-doped bismuth ferrite/bentonite) were prepared by a self-combustion method utilizing glycine as fuel and served for the removal of methyl orange (MO) from aqueous solutions. The ferrite-based adsorbents were characterized by the measurement of specific surface area (BET), scanning electron microscopy (SEM), Fourier Transform Infrared Spectroscopy (FTIR), X-ray diffraction (XRD). Both FTIR spectra of both ferrites showed three bands located around 419 cm^{-1}, 534 cm^{-1}, and 673 cm^{-1}, attributed to the stretching vibrations of Fe–O, MgO, and BiO, respectively. On the other hand, we observed an irregular and very porous structure in SEM images. Microcavities noticed on the surface of the two adsorbents were favorable for the good diffusion of dye molecules. BET analysis of the composites allowed us to measure their specific surface area. Thereby, we observed a mesoporous structure with a pore diameter of 15.5 nm. The different experimental parameters that affected the performance of this reaction such as temperature, contact time, initial dye concentration**,** and mass of adsorbent, were investigated. The point of zero charge pH (pH_{PZC}) was determined for the two adsorbents. Langmuir and Freundlich's adsorption models were employed to describe the equilibrium isotherms. The equilibrium time was found to be a function of the starting dye concentration in adsorption testing. The equilibrium adsorption for Mg-doped bismuth ferrite was formed after 300 min, whereas it was established after 180 min for Mg-doped bismuth ferrite-bentonite composite, according to the adsorption kinetic analysis. Furthermore, results revealed that pseudo-second order kinetics could properly characterize MO adsorption on both adsorbents. The adsorption isotherms confirmed that the methyl orange adsorption process on both the ferrite and its composite was successful. With a maximal adsorption capacity of 181.8 $mg.g^{-1}$ at 298 K, the Freundlich model perfectly reflected the adsorption of MO dye on the synthesized Mg-doped bismuth ferrite. The Langmuir model appeared to be the best fit for MO absorption on the Mg-doped bismuth-bentonite composite, with a maximum adsorption capacity of 188.8 $mg.g^{-1}$ in the same conditions. Adsorption was spontaneous and exothermic, according to the thermodynamic parameters associated with the sorbent/adsorbate system. The isosteric heat of adsorption was determined, showing that physisorption with weak intermolecular interactions between MO and the adsorbent surface was occurring.

Keywords Magnetic nanoferrite · Bentonite · Composite · Adsorption · Methyl orange

Abbreviations

$BiMgFeO_4$	Mg-doped bismuth ferrite
BiMgFeO4/Bentonite	Mg-doped bismuth ferrite-bentonite
MO	Methyl orange
FTIR	Fourier-transform infrared
SEM	Scanning electron microscopy
XRD	X-ray diffraction
S_{BET}	Brunauer–Emmett–Teller specific surface area
pH_{PZC}	The pH of point of zero charge

Sabrine Saad, Sarra Ben Amor and Amel Ben Slimane have contributed equally to this work.

✉ Amel Ben Slimane
amelbenslimane71@yahoo.fr

[1] Faculty of Sciences of Gafsa, University of Gafsa, Gafsa, Tunisia

1 Introduction

Dyes are used in a variety of industries, and their production is on the rise. However, their use in industries including cosmetics [1], foods [2], textiles [3], paper industries [4], medicines, and medical diagnostics [5] produces a lot of wastewater. Dyes are dangerous because their accumulation has major effects on ecosystems and, as a result, public health [6, 7]. Several wastewater treatment systems have been implemented selectively during the previous three decades, depending on the type of business and production. These include adsorption [8, 9] coagulation-flocculation [10], biological treatments [11], membrane separation [12], and chemical oxidation [13]. Adsorption techniques have been very effective in treating colored water, removing odors and organic pollutants [14]. Currently, activated carbon is the most widely used adsorbent [15], but the cost of preparation remains very high, which limits its use in developing countries. These problems have prompted us to investigate the processing of several types of adsorbents, such as magnetic materials [16]. Magnetic nanocomposites and magnetic core thin films have recently gained a lot of attention among the various natural and synthetic adsorbents employed. This is due to their great capacity to remove dyes and other organic and inorganic contaminants from aqueous solutions. They are also crucial for speeding up the separation rate and increasing the efficiency of water treatment. The ability to recycle magnetic nanoparticles for additional dye removal is, however, the greatest benefit of their employment. The magnetic insulation of harmful contaminants is developing as a viable approach to wastewater purification, and it has proven to be crucial in eliminating dyes more effectively than the traditional treatment method [17–19]. They are a dynamic emerging technology for inventive, practical, and high-performance electronics, as well as other interesting applications. Iron oxides, in particular, offer a variety of remarkable magnetic, electrical, and optical properties. These specific features have enhanced at the nanoscale, resulting in a growing interest in a wide range of applications. Various forms of ferrite nanoparticles [20, 21] have attracted attention in recent years due to their reactive surfaces. Other new ferrites include doped ferrites [22–27], which are multicomponent materials with better ferrites properties. These magnetic particles can potentially be used for a variety of purposes, including antibacterial activity [28], photodegradation [29], heavy metal removal [30], and dye adsorption [31].

Bentonite is montmorillonite type clay. An octahedral layer between two tetrahedral layers (T-O-T) forms the elementary sheet of montmorillonite. Si^{4+} ions are located inside a tetrahedron with oxygen atoms occupying the vertices. Al^{3+} ions are located inside an octahedron with four oxygen atoms and two hydroxyl ions occupying the vertices. The elementary sheets are of type 2/1 separated by water molecules and exchangeable cations [32, 33]. Numerous investigations on the alteration of clay minerals, such as bentonite, have been conducted in order to give them new functionalities. There have been a few studies on the design of magnetic bentonite for dye removal [34–37], but no investigations on the use of bismuth ferrite-modified bentonite for dye removal as far as we are aware.

For this purpose, we proposed the synthesis of a new-doped nanoferrite $BiMgFeO_4$ and its composite ($BiMgFeO_4$ / Bentonite) for the discoloration of water. The anionic dye Methyl Orange (MO), one of the most frequent colors used in textiles and considered as a model organic pollutant, was removed from wastewater using a self-combustion approach derived from the sol–gel method employing glycine as a fuel [38]. These materials were characterized by measuring the specific surface area by the BET method, scanning electron microscopy (SEM), Fourier transform infrared (FTIR), X-ray diffraction (XRD). We studied the adsorption of MO in a batch system by examining the effect of adsorbent dose, contact time, initial pH, and temperature. We used kinetic and thermodynamic adsorption, as well as several models of adsorption isotherms, including Langmuir and Freundlich models.

2 Materials and Methods

2.1 Chemicals Materials

All chemicals were purchased from Aldrich: Ferric nitrate nonahydrate ($Fe(NO_3)_3.9H_2O$), magnesium nitrate hexahydrate $Mg(NO_3)_2.6H_2O$, bismuth nitrate pentahydrate $Bi(NO_3)_3.5H_2O$, the Glycine $C_2H_5NO_2$, and hydrochloric acid (HCl, ACS reagent, 37%) were provided by Sigma-Aldrich, except Methyl Orange ($C_{14}H_{14}N_3NaO_3S$, supplied by Scharlu) and sodium hydroxide (BioXtra, ≥ 98%).

Bentonite was obtained from Jebel Ad-Darin sand from the Orbata formation in the Sened-Gafsa region (Tunisia). Its chemical composition showed maximum silica (SiO_2) contents on the order of 98%, with the presence of other oxides in small quantities [39].

2.2 Preparation of Bentonite

We introduced 100 g of the raw clay (bentonite) in a beaker containing a volume of 1L of distilled water; then stirred the mixture for 24 h at room temperature. The resulting suspension was dried at 80 °C until it reached a consistent weight, then crushed in a mortar, and finally sifted.

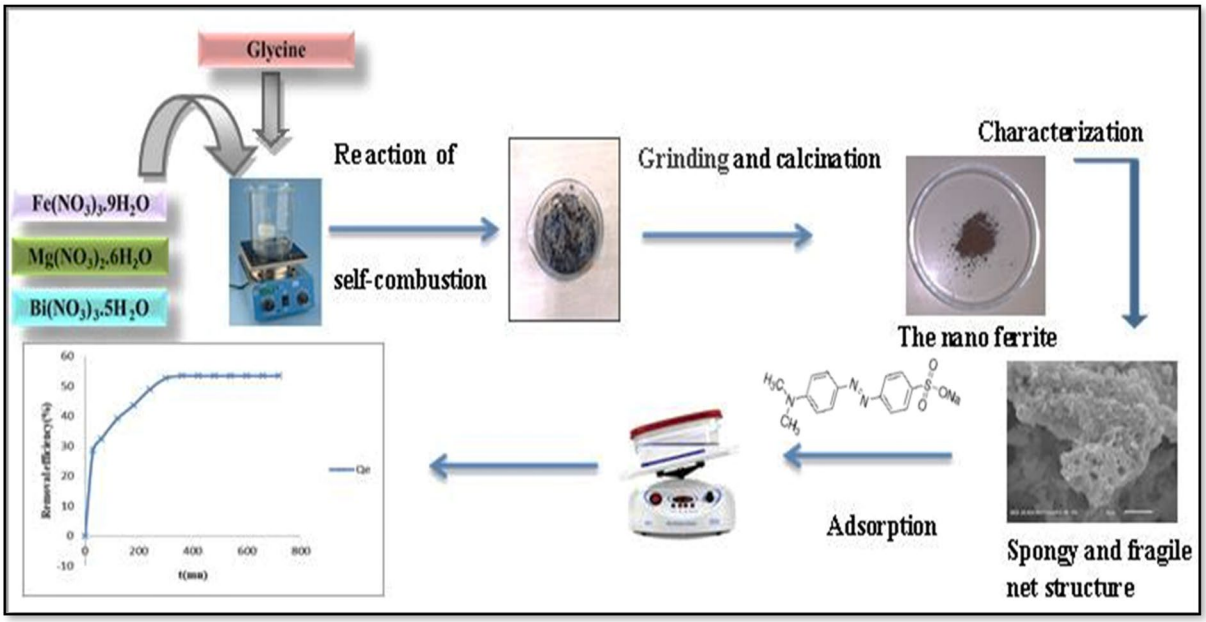

Fig. 1 The general strategy of preparation of Mg-doped bismuth ferrite Nanoparticles

2.3 Preparation of Nanomaterials

2.3.1 The General Strategy of the Work

The self-combustion process was used to make ferrite. Following that, we described it as having the property of chelating metals by forming a very stable soluble complex while preserving solvent volume. A more complete description can be found in Sect. 2.3.2. The whole process of adsorbent preparation and application is depicted in Fig. 1.

2.3.2 Preparation of $BiMgFeO_4$

Mg-doped bismuth ferrite powder was prepared by the self-combustion method [40]. For the preparation of Mg-doped bismuth ferrite powder, an equimolar concentration of bismuth nitrate pentahydrate ($Bi(NO_3)_3.5H_2O$), ferric nitrate nonahydrate ($Fe(NO_3)_3.9H_2O$) and magnesium nitrate hexahydrate ($Mg(NO_3)_2.6H_2O$) were dissolved independently in 50 mL of distilled water (Fig. 1). First, ferric nitrate nonahydrate $Fe(NO_3)_3.9H_2O$ and magnesium nitrate hexahydrate $Mg(NO_3)_2.6H_2O$ were mixed at 80–90 °C with thermal stirring until a homogenous mixture was formed, and then bismuth nitrate pentahydrate $Bi(NO_3)_3.5H_2O$ was added. The combustible agent (Glycine) was introduced after a few minutes respecting the following condition:

$$n_{glycine} = n_{Fe^{3+}} + n_{Mg^{2+}} + n_{Bi^{3+}}$$

where n is the mole number.

The homogeneous solution was mixed for 3 h at 80–150 °C with continuous thermal stirring. Afterward, it was evaporated to form a dry gel. Rapid heating was applied to this gel until it self-ignited. The rapid evaluation of a large volume of gas was accompanied by a significant loss of mass during combustion, leading to the formation of numerous foams and sparks, resulting in a bulky and fluffy product in the vessel. The direct transformation to the powder ferrite during combustion was obviously due to the heat generated by the exothermic reaction [41].

To obtain nanoparticles, the fine powder was crushed with a mortar. Finally, it was placed in an oven for 3 h at 180 °C to increase crystallinity and remove any remaining organic materials.

2.3.3 Preparation of the $BiMgFeO_4$/Bentonite Composite

$BiMgFeO_4$/Bentonite was synthesized by the auto combustion method: the raw materials used are iron (III) nitrate $Fe(NO_3)_3.9H_2O$, magnesium (II) nitrate $Mg(NO_3)_2.6H_2O$, bismuth (III) nitrate $Bi(NO_3)_3.5H_2O$, bentonite and glycine $C_2H_5NO_2$. The reagents were dissolved in distilled water according to a stoichiometric ratio that was determined, and the molar ratio between all components was set to one (except glycine).

The synthesis of $BiMgFeO_4$/Bentonite composite was carried out following the same pathway for the preparation of $BiMgFeO_4$ nanoferrite; however, the bentonite was introduced before the addition of the combustible agent.

2.4 Characterizations of the Nanoparticles

The synthesized samples were submitted to the FTIR analysis which was performed at room temperature over a range between 400 and 4000 cm^{-1} using KBr pellets solid (10% solid) in a Shimadzu 8400-S spectrometer.

Brunauer–Emmett–Teller (S_{BET}) specific surface area and pore structure parameters of synthesized material were obtained from N_2 adsorption–desorption measurements at 77 K using a Micromeritics ASAP 2020 instrument. Before measurement, the sample (approximately 40 mg) was degassed at 300 °C for 8 h.

Using a Powder X-ray diffraction (PXRD) D8 Advance Bruker two-circle diffractometer with a lynxeye detector, we acquired powder diffractograms. The dichromatic copper radiation (λ CuK α_1/ α_2) was utilized by the θ-2θ scan in the 2θ angular range of 5–70°. The wavelengths were $\lambda_{K\alpha1} = 0.154\ 060$ nm and $\lambda_{K\alpha2} = 0.154\ 439$ nm. Full diffraction power of 40 mA /40 kV with 0.02° Δθ step and an exposure time of 2 s time per step.

The morphology of the samples has been assessed using Scanning electron microscopy (SEM) micrographs obtained on a ZEISS-ULTRA55 SEM microscope.

The pH of point of zero charge (pH_{PZC}) was determined by the pH drift method [42]. Briefly, many aqueous solutions of NaCl (0.1 M) with different pH from 2 to 12 were obtained by addition of hydrochloric acid and sodium hydroxide. Then, 0.15 g of the nanoferrite was added to the NaCl solutions. We set the pH to between 2 and 12, and the suspension reached equilibrium after 2.5 h of agitation. The final measured pH was determined as a function of the original pH. The pH value that intersects the pH (final) = pH (initial) line is known as the zero charge point (PZC) for the nanomaterial. However, these various pH tests were all carried out simultaneously.

2.5 Batch Adsorption

2.5.1 Analytical Method

Following the adsorption experiments, the concentration of MO was determined by a Beckman UV/Vis DU 800 Spectrophotometer at a maximum wavelength of $\lambda_{max} = 465$ nm. The equilibrium adsorption capacity Q (mg. g^{-1}) was calculated according to Eq. (1):

$$Q = \frac{(C_0 - C_e)V}{m} \tag{1}$$

With C_0 is the initial concentration of MO, C_e (mg. L^{-1}) is the equilibrium concentration of MO, V (L) is the volume of the solution, and m (g) is the mass of the nanoferrite.

2.5.2 Effect of Initial pH, Adsorbent Dose and Temperature

MO adsorption tests were realized in batch mode to examine the effects of adsorbent dose, initial pH, and temperature. To evaluate the effect of initial pH, we have performed experiments at room temperature using 10 mL of MO dye solution (50 mg. L^{-1}). A fixed dose of adsorbent (10 mg) was added, and the pH was adjusted from 2 to 12 by adding HCl or NaOH solutions (0.1 mol**.** L^{-1}) using a pH meter. The solutions were shaken for 720 min in a temperature-controlled water bath shaker at 60 rpm. The samples were then filtered, and the concentration was determined.

In order to determine the most favorable adsorbent dosage, we varied the adsorbent dosage from 5 to 150 mg. The experiments were carried out according to the same approach and conditions as previously stated.

To assess the influence of the temperature on the adsorption process of the different adsorbents, we mixed 100 mL of MO solution (C = 50 mg. L^{-1}) with 50 mg of the considered adsorbent and observed the reaction at different temperatures (2, 7, 15, 25, 40, 60 and 75 °C).

2.5.3 Adsorption Kinetic Studies

The following steps were adopted to evaluate the influence of contact time on adsorption: 50 mg of adsorbent was stirred with 100 mL of MO solution (50 mg. L^{-1}) at room temperature (25 °C) and for the appropriate contact time, which can range between 0 and 720 min.

2.5.4 Adsorption Isotherms

Experiments were performed by varying the initial MO concentration (20-200 mg.L^{-1}), for 720 min. Each test utilized an adsorbent mass of 50 mg. The experimental points were examined using Langmuir's Eq. (2) [43], and Freundlich Eq. (3) [44]:

$$Q_e = \frac{K_L C_e}{1 + K_L C_e} \tag{2}$$

$$Q_e = K_F C_e^{\frac{1}{n}} \tag{3}$$

With K_L being the Langmuir equilibrium constant associated with the adsorption affinity, Ce is the concentration at the equilibrium; Q_e is the adsorbed amount and C_e is the equilibrium concentration; K_F is the Freundlich constant (heterogeneity factor), and 1/n is the Freundlich coefficient. n related to sorption affinity and K_F is related to the sorption capacity.

3 Results and Discussions

3.1 Characterization of the Nanoferrites with Infrared Spectrum

The analysis of the infrared spectrum of $BiMgFeO_4$ (Fig. 2a) showed the existence of a wide absorption band at 3734 cm^{-1} which corresponded to the stretching vibrations of internal OH groups. The band located between 1600 and 1700 cm^{-1} could be attributed to the valence vibrations of the OH group of the constituent water, in addition to the stretching vibrations of the adsorbed water, and found at 1634 cm^{-1}. As well, the peak at 1384 cm^{-1} corresponded to the vibrations of the nitrate coming from the iron nitrate nonahydrate, which is a constituent of the ferrite.

In general, the infrared spectrum of spinel ferrites exhibited two main characteristic bands associated with intrinsic vibrations of the oxygen bonds with metal cations on the two subarrays [45, 46].

Indeed, the metal–oxygen bands were located in the range 400–1000 cm^{-1}, the first band being present on the spectrum around 419 cm^{-1} that corresponded to the Fe–O stretching vibration. The second band was at 534 cm^{-1} and was due to the elongation of the Mg-O bond and the third band at

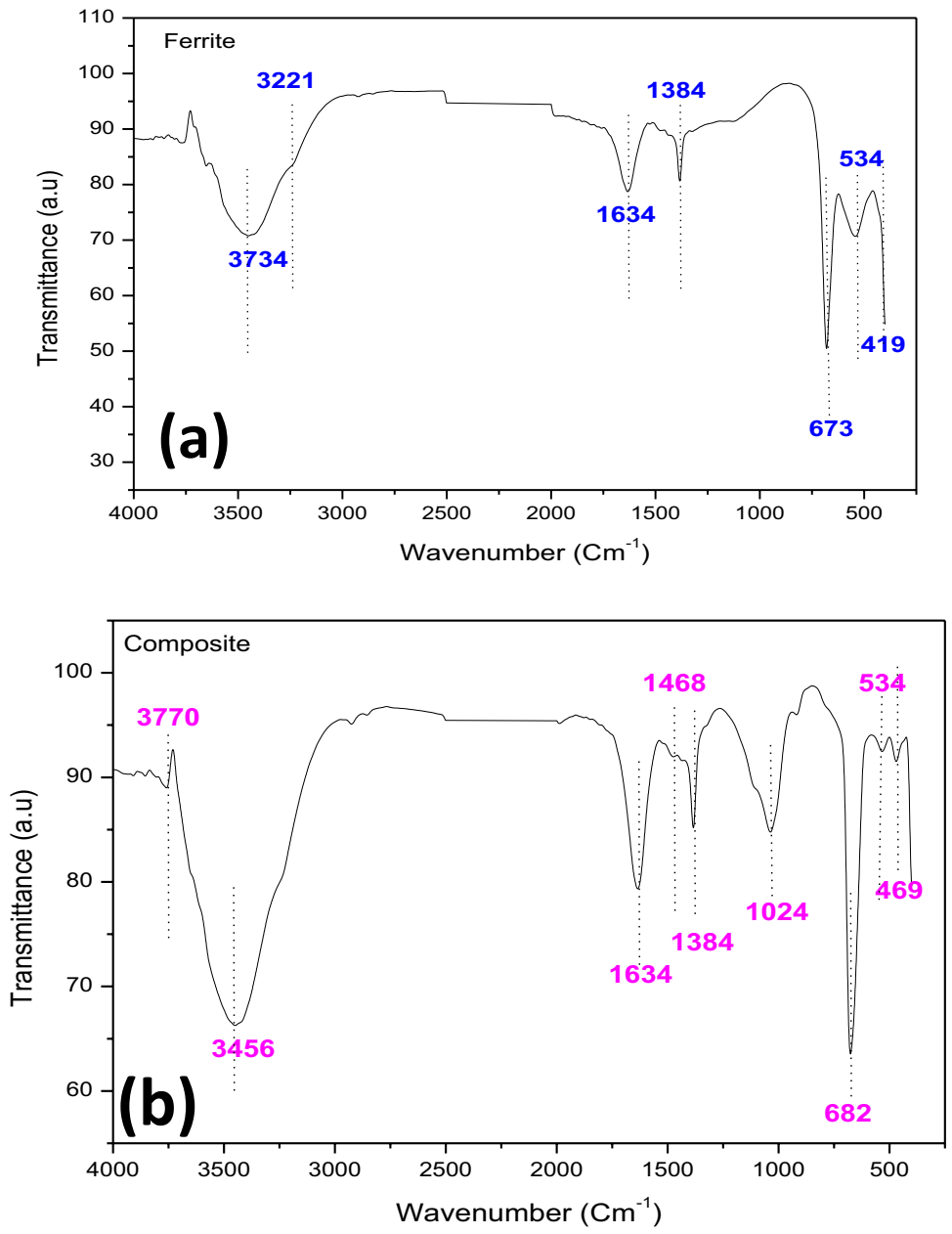

Fig. 2 FTIR spectra of (**a**) $BiMgFeO_4$ ferrite, and (**b**) $BiMgFeO_4$/Bentonite composite

673 cm^{-1} which corresponded to the Bi-O stretching vibration [47].

The analysis of the infrared spectrum of the ($BiMgFeO_4$/Bentonite) composite (Fig. 2b) allowed to observe the presence of an intense band at 3456 cm^{-1} relating to an elongation vibration of the O–H group derived from the bentonite present in the composite. The little band around 3700 corresponded to the presence of the $BiMgFeO_4$ nanoferrite**,** which corresponded to the elongation vibrations of internal OH groups. The band at 1634 cm^{-1} was due to the deformation vibrations of the O–H bond of the constituent water and to the deformation vibrations of the bonds of the water molecules adsorbed during the preparation of the composite. The band at 1384 cm^{-1} corresponded to the vibrations of the nitrate. The signal detected around 1468 cm^{-1} corresponded to sodium carbonate Na_2CO_3 derived from the bentonite. We observed as well, a significant signal at 1024 cm^{-1}**,** which justified the presence of silica due to the stretching vibration of Si–O–Si group of kaolinite or quartz. Moreover, bands of the metal–oxygen were located around 400–1000 cm^{-1} and attributed to the intrinsic stretching vibrations of the metal. The first band was located on the spectrum at 682 cm^{-1} and corresponded to the stretching vibration of Bi-O [48]. The second band was at 469 cm^{-1} and was due to Fe–O bond elongation. Finally, the presence of a band of low intensity around 534 cm^{-1} corresponded to a stretching vibration of Mg-O present in the ferrite.

3.2 Characterization of the Nanoferrites with Scanning Electron Microscope (SEM) Micrographs

Figure 3 displays SEM images of ferrite (Fig. 3a–c) and its composite (Fig. 3d–f) at various magnifications.

On the surface of the ferrite, nodular and non-homogeneous particles of various sizes could be seen (Fig. 3b). On the other hand, SEM images showed an irregular and very porous structure favorable for good diffusion of dye molecules, with a large percentage of voids, and different pore sizes present in the samples. These voids could generally be explained by the release of a large amount of gases (NO, NO_2, CO, NH_3 and H_2O) during the combustion process [49, 50] (Fig. 3a). Indeed, the release of associated gas resulted in a highly porous structure [51]. Microcavities observed on the surface of the adsorbent, seemed to indicate a very irregular structure porous favorable for good diffusion of dye molecules.

The $BiMgFeO_4$/Bentonite exhibited important spongy structure (Fig. 3d–f), which was due specifically to the effect of the combustion agent used (glycine). The pores of various sizes observed in the samples were attributed to the voids**,** which corresponded to the release of a large quantity of gases during the combustion reaction. Since the release of associated gas resulted in a highly porous structure with non-homogeneous and agglomerated particles. This resulting porosity presented a very important factor for the evolution of adsorption.

The incorporation of bentonite during the preparation of the ferrite-derived composite has helped to modify the morphological structure of the latter's surface, as well as the number and size of cavities and pores in the nanocomposite. This implied that the composite thus prepared, would be more subject to the adsorption of the molecules of the dye. The surface morphology of mineral substrates, nanoferrite ($BiMgFeO_4$), and its $BiMgFeO_4$/Bentonite composite were compared at the same magnification (first at 5 µm scale, and then at 50 µm scale). There was evidence of surface enrichment of the produced composite through greater porous cavities and an enhanced spongy structure of the adsorbent, as well as its heterogeneity. This phenomenon enhanced the dye adsorbing capacity of the composite.

3.3 Characterization of Nanoferrites with X-ray Diffraction (XRD)

Figure 4 displays the diffractogram of the composite. The peak positions are reported and assigned to Fe_3O_4, MgO and Bi_2O_3 identified in the composite. For comparison, diffraction patterns of the composite and pure Bi_2O_3 are shown in the Supplementary Information. There are also several minerals such as kaolinite ($Al_2Si_2O_5(OH)_4$), which corresponded to $2\theta = 12.37°$ and to $2\theta = 24.92°$. The peaks appearing towards $2\theta = 12.31°$, $2\theta = 26.59°$ and $2\theta = 29.34°$ corresponded to the calcite Ca (CO_3) and mainly the quartz (SiO_2) present in large proportions in the bentonite.

3.4 Measurement of the Specific Surface Area of the Composites by BET Analysis

The specific surface area and the distribution and pore size were determined from adsorption–desorption isotherms of liquid nitrogen at − 195° C (77 K) [52]. Because of the limitations in N_2 adsorption, this approach can only assess the material's external surface [53]. The composite results are provided below (Fig. 5).

Figure 5 suggested that the isotherm plot recorded with $BiMgFeO_4$/Bentonite composite belongs to the type IV adsorption isotherm in the classification of Brunauer, Deming, Deming and Teller (BDDT). The analysis of adsorption and desorption isotherms of dinitrogen at low temperatures of the materials revealed at low pressures a significant adsorption followed by a gradual increase in the amount of quantity of adsorbed gas, which was rather apparent for the composite compared to that of ferrite. Then, at a relatively high pressure, a distinguished capillary condensation phenomenon was observed during desorption by the presence

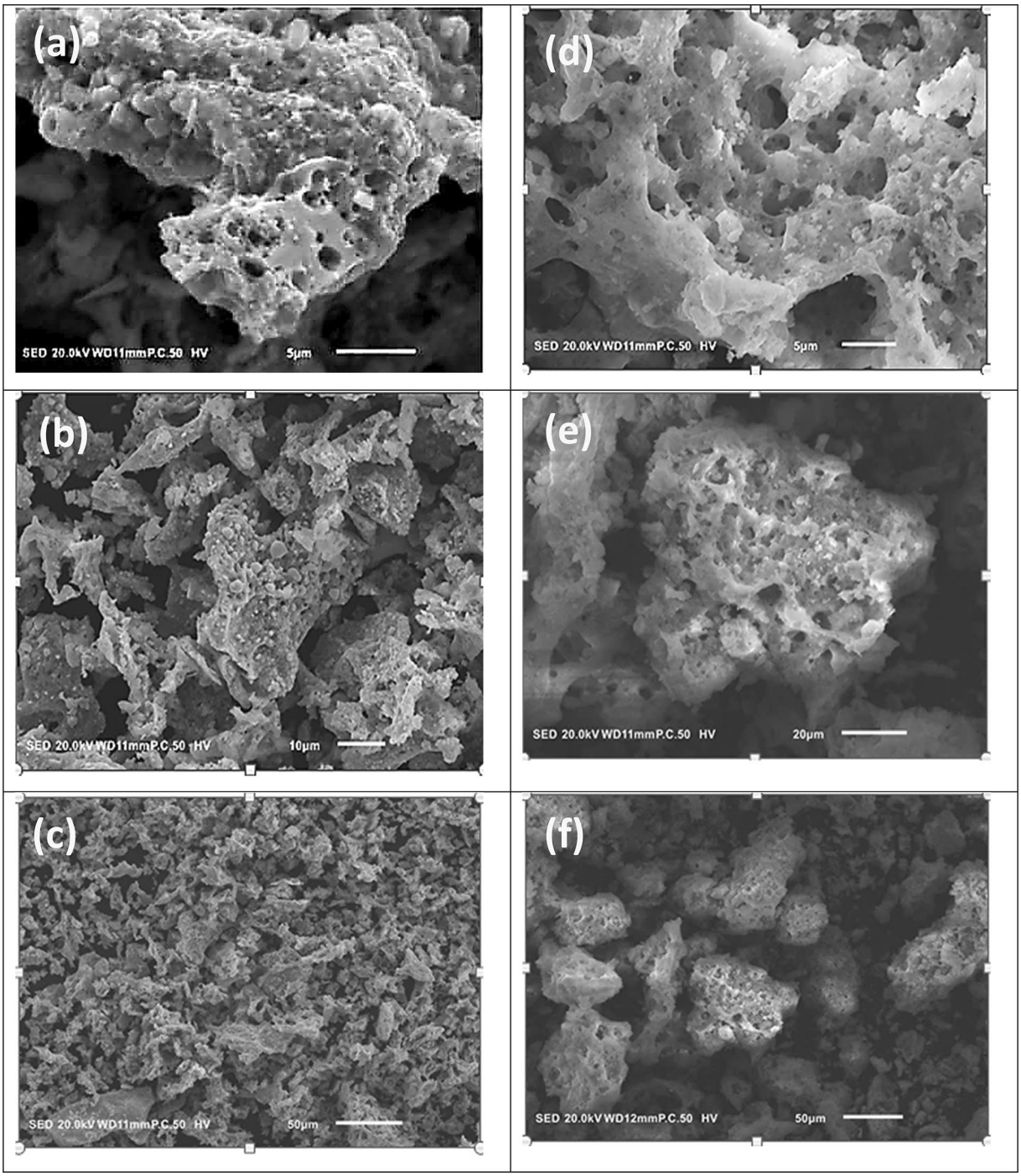

Fig. 3 SEM images of $BiMgFeO_4$ nanoferrite powder (**a**, **b**, **c**), and $BiMgFeO_4$/Bentonite composite (**d**, **e**, **f**) at different magnifications

of a hysteresis loop type H4 large enough for the composite [54].

The volume of N_2 adsorbed by $BiMgFeO_4$/Bentonite composite was quite high, and reached 34 cm^3/g at high pressure, due to the increase of the specific surface. The specific surface area calculated using the BET equation was ~ 25.0 m^2/g for the composite. The size of the pore volume in the (BiMgFeO4/Bentonite) composite was 0.0456 cm^3/g, and the pore diameter was 15.5 nm (Table 1). The mean volumes of the pores as well as their diameters of the powder were calculated by the method of Barrett—Joyner—Halenda BJH [55]. The composite was a mesoporous material with a surface area of 25 m^2/g and diameters of the pores ranged from 2 to 50 nm. This mesoporous structure was well suited

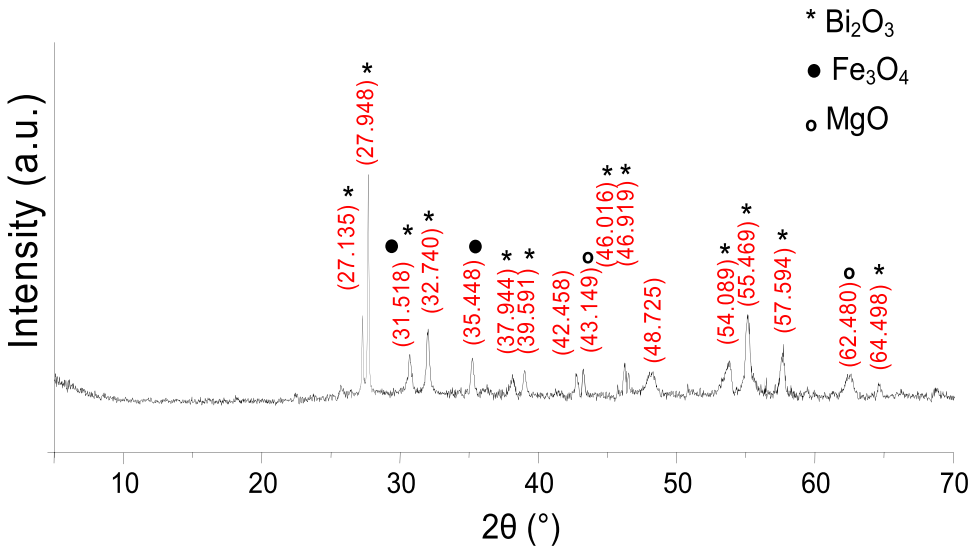

Fig. 4 XRD pattern of the composite material

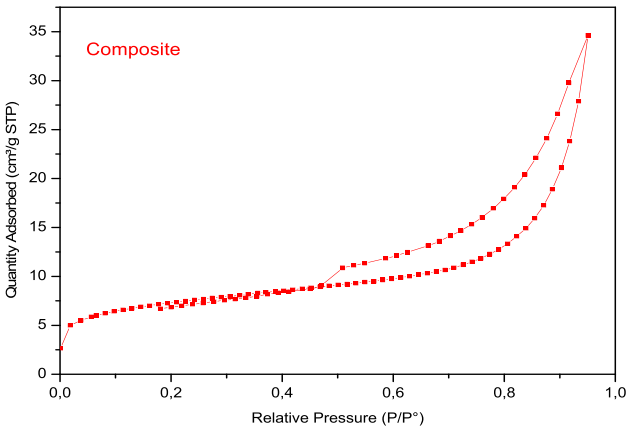

Fig. 5 Adsorption and desorption isotherms of N_2 on $BiMgFeO_4$/Bentonite composite

Table 1 Textural and morphological of the $BiMgFeO_4$/Bentonite

Adsorbent	Pore volume (cm^3/g)	Pore diameter (nm)	Specific surface area SBET (m^2/g)
Composite	0.0456	15.5	25.0

to the removal of the MO anionic dye. The pores observed on the surface of the adsorbents showing small diameters, confirmed that it was indeed a type IV isotherm.

3.5 Determination of Point of Zero Charge pH (PZC) for the Nanoferrites

The adsorbent's surface and nature have a significant impact on the adsorption of any sort of ion at different pH levels. The pHpzc of the adsorbent can be used to describe its surface charge. Below this value when pH < pHpzc there is an excess of positive charge on the surface, so that anions can be adsorbed. Conversely, beyond this value at pH > pHpzc, the surface charge would be negative so that the cations can be adsorbed. [56].

The pH_{PZC} of the nanoferrite is determined by intersecting the experimental curve of final pH versus initial pH with the bisector (final pH = initial pH) [57].

As shown in Fig. 6a, for $BiMgFeO_4$ the pH_{PZC} (nanoferrite) is 7.6. If the pH of the solution is less than 7.6, the surface of the adsorbent is positively charged and anions would be adsorbed at this pH zone. The adsorbent's surface functional groups would be protonated by excess H + protons from the solution, and the support would attract negatively charged adsorbate.

According to the curve (Fig. 6b), the pH_{PZC} ($BiMgFeO_4$/Bentonite) = 8.2. This indicates that when solution pH is below 8.2, the surface of the ($BiMgFeO_4$/Bentonite) composite is positively charged via the protonation of the hydroxyl group bonded to the metal.

($M–OH + H^+$ $M–OH_2^+$, where M is metal).

When the solution pH rises over pH_{PZC}, the surface of the composite becomes negative due to the deprotonation of the hydroxyl group linked to the metal.

($M–OH + OH^-$ $M–O^- + H_2O$).

3.6 Batch Adsorption Experiments

3.6.1 Effect of initial pH on the Adsorption of Methyl Orange

Figure 7 displays the variation of the adsorbed amount of the MO anionic dye on $BiMgFeO_4$ nanoferrite and on $BiMgFeO_4$/Bentonite composite versus pH. At acidic pH levels, there was a high MO adsorption capacity. This might

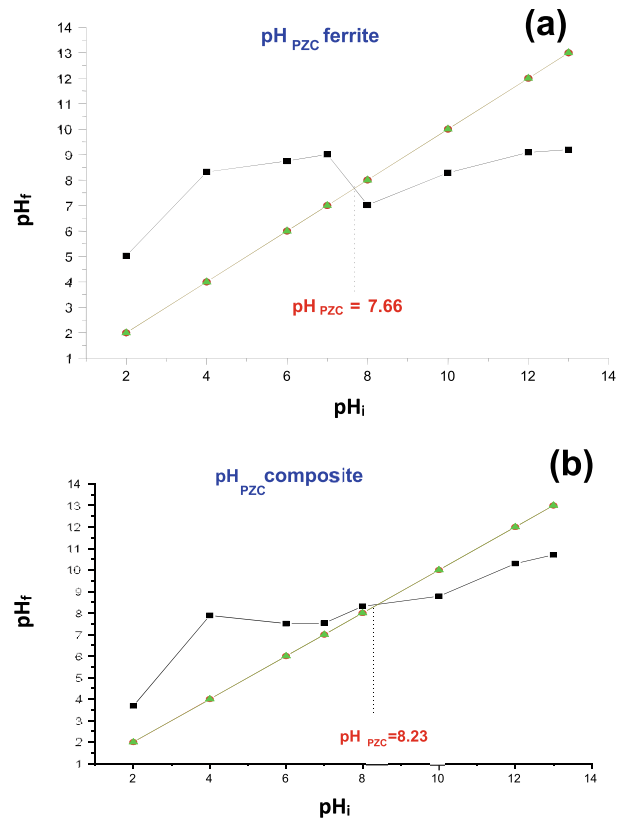

Fig. 6 Zero charge point pH_{PZC} of the $BiMgFeO_4$ nanoferrite (**a**) and $BiMgFeO_4$/Bentonite composite (**b**)

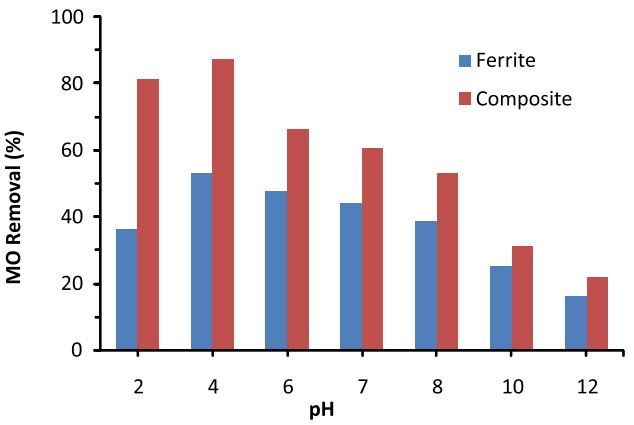

Fig. 7 pH effect on the adsorption of methyl orange on the $BiMgFeO_4$ nanoferrite (Filled Square) and the $BiMgFeO_4$/Bentonite composite (Filled Square) ([MO] = 50 mg. L^{-1}, adsorbent amount = 10 mg, time = 720 min, T = 25 °C)

be explained by the pH_{PZC}, which is 7.6 for the produced ferrite and 8.2 for its composite.

3.6.2 Effect of the Adsorbent Dose on the Adsorption of Methyl Orange

As shown in Fig. 8, when the adsorbent dose was increased, the MO removal efficiency increased, whereas the MO adsorption capacity decreased. Because adsorption sites were entirely accessible for MO at low adsorbent dosage, the adsorption capacity was increased. However, at high adsorbent doses, the majority of the low-energy adsorption sites were first occupied. Consequently, the accessibility of high-energy adsorption sites significantly decreased, and adsorption capacity was reduced [58]. Moreover, the higher the adsorbent dose, the more likely collisions and agglomeration between solid particles occurred, leading to a decrease in total surface area and ferrite adsorption capacity for MO.

Increasing the mass of the adsorbent offers an increased number of available adsorption sites and therefore increased amount of adsorbed dye [59]. While the decrease of MO adsorption could be explained by the saturation of adsorption sites [60]. However, the percentage of the solution dye decolorization was higher with the $BiMgFeO_4$/Bentonite composite. It reached 92% for 1.5 g of adsorbent in 100 mL of solution, while it was 72% for $BiMgFeO_4$ nanoferrite as adsorbent with the same dose.

3.6.3 Effect of the Contact Time on the Adsorption of Methyl Orange Using Nanoferrites

The test of discoloration of MO by adsorption on the $BiMgFeO_4$ ferrite and the ($BiMgFeO_4$/Bentonite) composite (Fig. 9) was carried out by following the contact time of the adsorption equilibrium, where a substrate saturation state was established. It is considered the most critical parameter in the development of an economical wastewater treatment system [61]. In fact, the contact time is fundamental for the determination of the maximum quantity of adsorption. The adsorption capacity or removal rate was calculated from Eq. (4)

$$\%\text{Removal} = \frac{C_0 - C_t}{C_0} \times 100 \quad (4)$$

With C_0: initial concentration and C_t: concentration at time t.

As shown in Fig. 9, when $BiMgFeO_4$ nanoferrite was the adsorbent, the removal efficiency (percentage) of MO increased as the contact time varied from 20 to 300 min before reaching a steady state. Consequently, the equilibrium time was determined to be 300 min. At this stage, the amount of dye desorbed from the adsorbent was in a dynamic equilibrium state with the amount of dye adsorbed on the adsorbent.

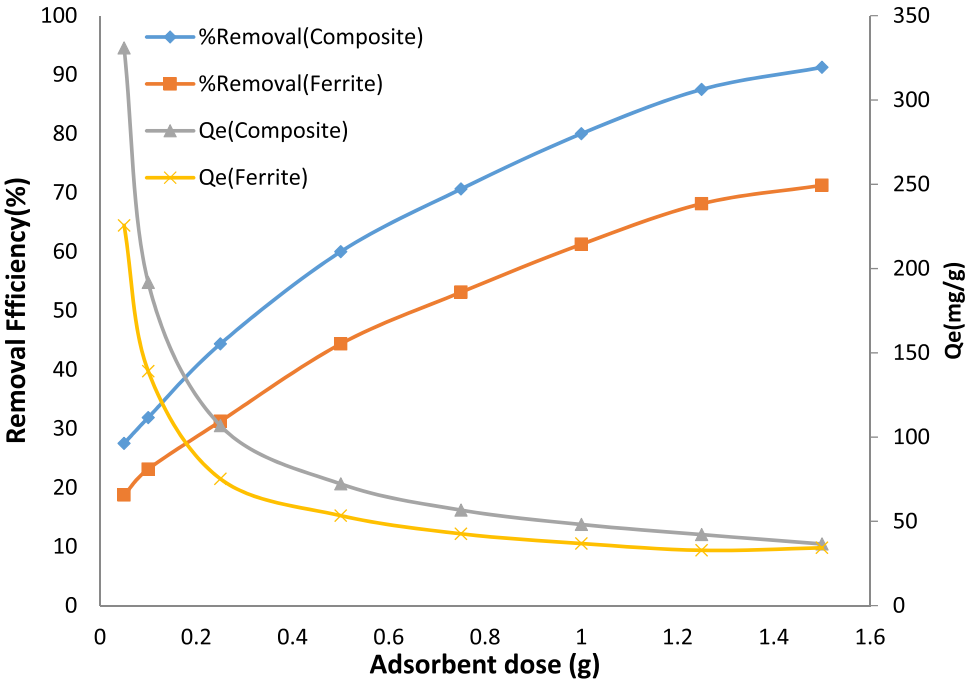

Fig. 8 The effect of ($BiMgFeO_4$) nanoferrite and the ($BiMgFeO_4$/Bentonite) composite dose on the adsorption of Methyl Orange. ([MO] = 50 mg. L^{-1}, time = 720 min, T = 25 °C)

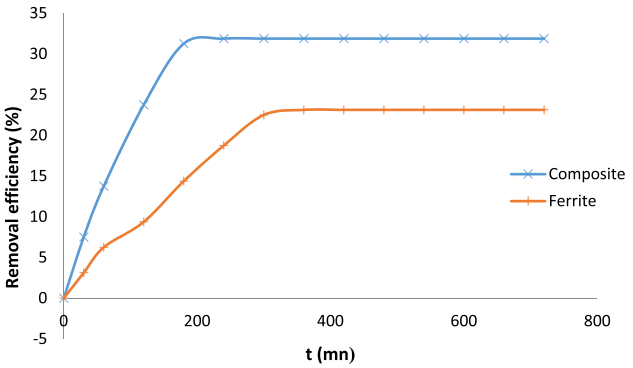

Fig. 9 The effect of the contact time on the adsorption of methyl orange by ($BiMgFeO_4$) nanoferrite and $BiMgFeO_4$/Bentonite composite. ([MO] = 50 mg. L^{-1}, Adsorbent amount = 50 mg, T = 25 °C)

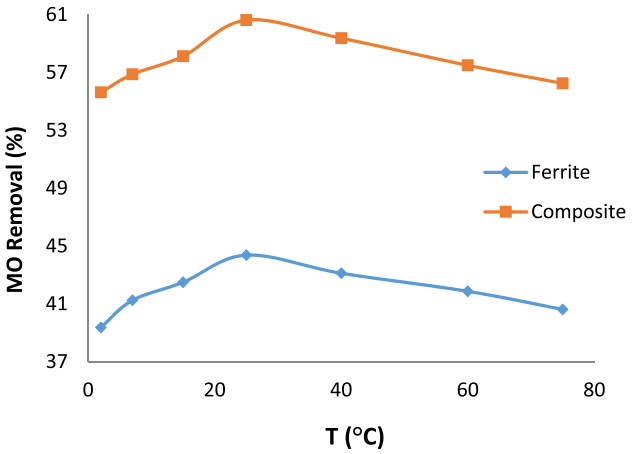

Fig. 10 Effect of temperature on MO dye adsorption on the two adsorbents. ([MO] = 50 mg. L^{-1}, adsorbent amount = 50 mg)

The adsorption was fast during the first minutes of the reaction because at the beginning of adsorption, the number of active sites available on the surface of the adsorbent was much more important than the number of sites remaining after a certain time. For high contact times, the molecule needed time to diffuse inside the pore of the adsorbent [62], for the rest of the quantity not adsorbed is interpreted by the saturation of the surface of the adsorbent (all the sites of adsorption were occupied).

On the other hand, the removal efficiency (percentage) of MO dye by the $BiMgFeO_4$/Bentonite composite increased as the contact time progressed to reach 180 min before becoming constant. Therefore, the equilibration time of 3 h was sufficient in this case as maximum adsorption occurred during this time. It was due to the aggregation of the dye particles with increasing contact time, which made it almost impossible to diffuse deeper into the adsorbent structure at higher energy sites. This aggregation canceled out the influence of contact time as the pores filled in and began to offer resistance to diffusion of aggregated dye molecules into the adsorbents [63]. The experimental results indicated that the optimal value of contact time for OM removal was lower with the composite. This fact proves that the addition of bentonite increased the percentage of dye adsorption and decreased the adsorption contact time.

Table 2 Pseudo-first-order and pseudo-second-order models parameter

Adsorbent	Pseudo-first order model				Pseudo-second order model		
	R^2	K1 (mn^{-1})	Q1 (mg/g)	Q exp (mg/g)	R^2	K2 (g/mg/mn)	Qexp.(mg/g)
$BiMgFeO_4$	0.952	0.0095	41	52.6	0.996	0.00058	56.1
$BiMgFeO_4$/Bentonite	0.0239	96.9	72.9	0.997	0.00063	75.7	0.92

3.6.4 Influence of the Temperature on the Adsorption of Methyl Orange by Nanoferrites

Figure 10 displays the variation of temperature versus the removal efficiency (percentage) of methyl orange on $BiMgFeO_4$ nanoferrite, and the $BiMgFeO_4$/Bentonite composite. Due to the obvious decrease in solution viscosity, rising temperature was known to enhance the rate of diffusion of adsorbate molecules through the outer boundary layer and into the interior of the adsorbent particles [64].

Figure 10 reveals that at 25 °C, the maximum removal rate of the MO dye from $BiMgFeO_4$ nanoferrite was 44.7%. At the same temperature, it was 60.6% when the $BiMgFeO_4$/Bentonite composite was used as an adsorbent.

From the comparison of the two curves in Fig. 10, room temperature (25 °C) was the most suitable temperature for the maximum removal of the methyl orange anionic dye by both materials. A rise in temperature was not favorable for the adsorption phenomenon; this could prove that it was an exothermic mechanism.

3.6.5 Adsorption Kinetics

The thermodynamic equilibrium between the adsorbate in the liquid phase and the adsorbate fixed to the solid was attained at a rate that depended not only on the rate at which the components diffused in the adsorbent and fluid but also on the adsorbent-adsorbate interaction. We were able to examine the effect of contact time on dye retention by studying dye adsorption on nanoferrite as a function of time.

For this purpose, two models have been applied to describe the mechanism of the adsorption kinetics of methylene blue on wood ash: the pseudo-first order (Eq. 5) and the pseudo-second order (Eq. 6) [65, 66]:

$$\ln(Q_{ads} - Q_t) = \ln Q_{ads} - K_1 t \tag{5}$$

$$\frac{t}{Q_t} = \frac{1}{Q_e^2 \times K_2} + \frac{t}{Q_e} \tag{6}$$

Qe (mg / g) is the equilibrium adsorption capacity, Q_t (mg/g) is the adsorption capacity at time t. K_1 (mn^{-1}) is the constant of the pseudo-first order model, and K_2 ($g.mg^{-1}.mn^{-1}$) constant of the pseudo-second order model.

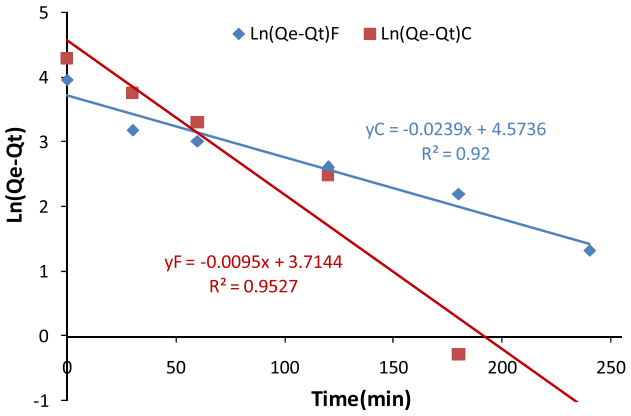

Fig. 11 Pseudo-first order model applied to the adsorption of MO on the Ferrite and on the Composite (C = Composite; F = Ferrite)

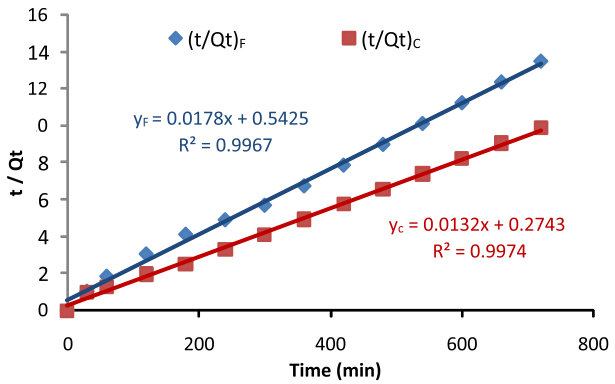

Fig. 12 Pseudo-second order model applied to the adsorption of MO on the Ferrite and on the Composite (C = Composite; F = Ferrite)

The results in Table 2 demonstrate that the experimental adsorbed quantity differed from the estimated amount for the pseudo-first order kinetic adsorption reaction on $BiMgFeO_4$ ferrite and on $BiMgFeO_4$/Bentonite composite. Similarly, the values of correlation coefficient (Respectively $R^2 = 0.952$ and 0.92) were slightly away from the unit. Therefore, the adsorption kinetic of the MO did not obey to a pseudo-first order kinetic. In contrast, higher correlation coefficients R^2, close to unit, were obtained for the ferrite and its composite ($R^2 = 0.996$ and 0.997, respectively) for the pseudo-second

order kinetic adsorption. The results better fit second order kinetic model for the adsorption of MO.

The pseudo-first order constants were determined by extrapolation of the curve representing the variation of Ln ($Q_e - Q_t$) as a function of time t (mn) (Fig. 11).

Otherwise, Fig. 12 clearly illustrates the pseudo-second order kinetic model results for the adsorption of Methyl orange dye on the two adsorbents. The two quantities K_2 constant of the pseudo-second order model, and Qe the adsorbed capacity at equilibrium, corresponded respectively to the y-intercept and the slope of the line that represented the variation of t/Q_t as a function of the time t (min).

3.6.6 Adsorption thermodynamics

The adsorption thermodynamic constants are the standard enthalpy variation (ΔH^0), the standard Gibbs free energy variation (ΔG^0), and the standard entropy variation (ΔS^0). They were calculated as following equations, Eq. (7) and Eq. (8) [67].

$$\Delta G_0 = -RT\ln K_L \tag{7}$$

$$\ln K_L = \frac{\Delta S_0}{R} - \frac{\Delta H_0}{RT} \tag{8}$$

where T is the absolute temperature in Kelvin, K_L (L. mol^{-1}) as Langmuir's constant, R is the universal gas constant (8.314 J. mol^{-1} K^{-1}) and ΔH^0 and ΔS^0 were calculated from the linear plot slope and the intercept of $\ln K_L = f(1/T)$ (Fig. 13). Table 3 reports ΔG^0 values; all are negative which indicates thermodynamically favorable process. When the temperature increased, the values of standard free enthalpy variation decreased, it is a confirmation of the exothermic nature of the adsorption process.

The ΔH^0 values reported in Table 3 were negative indicating that the adsorption reaction of methyl orange (MO) on nanoferrite and composite was exothermic. In addition, the positive values of ΔS_0 showed the increase in molecular disorder at the solid/liquid interface of the adsorption process and an increase in the degree of freedom of the adsorbed molecules. ΔH_0 and ΔS_0 were of opposite sign; therefore, we did not observe a modification in the sign of the free enthalpy variation or a remarkable variation in its value by varying the temperature.

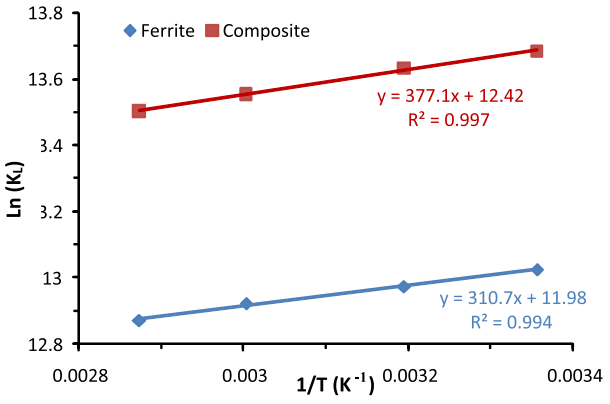

Fig. 13 Ln (*KL*) versus (1/T) for MO adsorption on $BiMgFeO_4$ nanoferrite and on $BiMgFeO_4$/Bentonite composite

3.6.7 Adsorption Isotherm of Methyl Orange (OM)

The experimental results were examined using Langmuir (Eq. 9) and Freundlich (Eq. 11) models. Langmuir isotherm model is one of the most frequent isotherms used for the adsorption in order to evaluate the maximum adsorption capacity of an adsorbate on an adsorbent. It requires that adsorption occurs on monolayer coverage of adsorbate over a homogenous adsorbent surface. Also, this model assumes that adsorption performs on specific homogeneous and energetically identical sites [68].

$$\frac{1}{Q_e} = \frac{1}{Q_m} + \frac{1}{Q_m K_L C_e} \tag{9}$$

where K_L (L.mg^{-1}) is the Langmuir equilibrium constant related to the affinity of adsorption, Q_m (mg. g^{-1}) is the maximum adsorption capacity in monolayer, and Ce is the concentration at equilibrium.

The dimensionless equilibrium constant for the Langmuir isotherm can be expressed as (Eq. 10) [69]:

$$R_L = \frac{1}{1 + K_L C_0} \tag{10}$$

(Eq. 10) defines the separation factor, R_L [70–74]. The adsorption isotherm is unfavorable when $R_L > 1$, it is linear

Table 3 Thermodynamic parameters for the adsorption of MO on the $BiMgFeO_4$ ferrite and ($BiMgFeO_4$/Bentonite) composite

Adsorbent	ΔH^0 (kJ. mol^{-1})	ΔS^0 (J^{-1} mol^{-1} K^{-1})	ΔG^0 (kJ. mol^{-1})				
			275 K	288 K	298 K	333 K	348 K
$BiMgFeO_4$	− 2.583	99.626	− 29.308	− 31.003	− 32.269	− 35.777	− 37.239
$BiMgFeO_4$/Bentonite	− 3.135	103.259	− 30.811	− 32.512	− 33.898	− 37.521	− 39.064

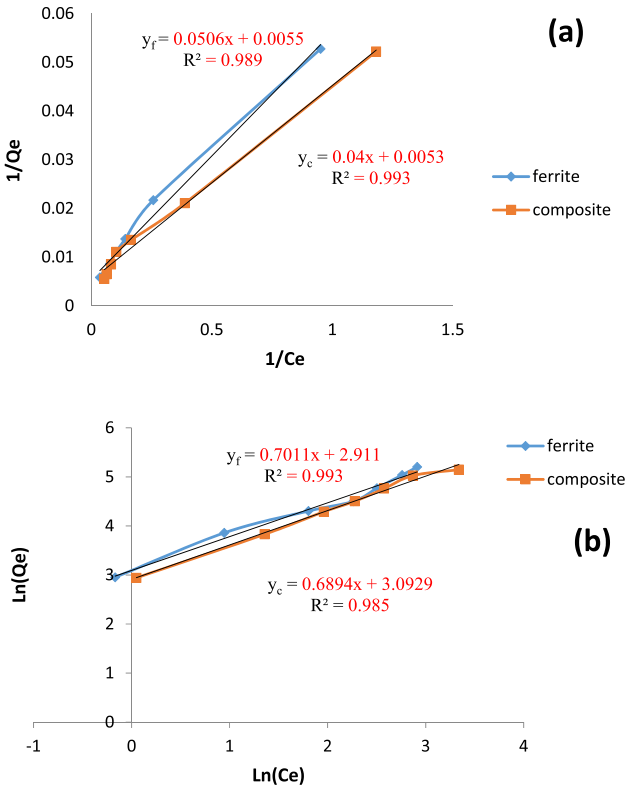

Fig. 14 Langmuir (**a**) and Freundlich (**b**) isotherms for the adsorption of MO on ferrite. (Blue filled diamond) and composite (Orange filled square)

Table 4 Adsorption Equilibrium parameters for Langmuir and Freundlich Isotherms

Langmuir Isotherm parameters			Freundlich Isotherm parameters		
Item	$BiMgFeO_4$	$BiMgFeO_4$/Bentonite	Item	$BiMgFeO_4$	$BiMgFeO_4$/Bentonite
Qm (mg/g)	181.8	188.8	1/n	0.7011	0.3234
KL (L/g)	0.1087	0.1325	Kf (L/g)	18.38	22.0409
RL	0.1554	0.131	R2	0.993	0.985
R2	0.988	0.9931			

when $R_L = 1$, it is favorable when $0 < R_L < 1$ and it is irreversible when "$R_L = 0$".

The Freundlich model assumes heterogeneous surface energy. This model is widely used to describe multilayer adsorption [75]. The no-linear form of the Freundlich can be expressed as follows:

$$\mathrm{LnQ_e} = \mathrm{LnK_F} + \frac{1}{\mathrm{n}}\mathrm{LnC_e} \tag{11}$$

where K_F is the Freundlich constant (heterogeneity factor), and 1/n is the Freundlich coefficient. n is related to the sorption affinity and K_F is related to the sorption capacity. When the coefficient n is between 1 and 10, the adsorption performance of an adsorbent improves [76–78].

Figure 14 depicts the adsorption isotherms for both adsorbents, and the table below (Table 4) displays the results of the modeling studies of the adsorption isotherms for the two models (Langmuir and Freundlich) and the correlation coefficients (R^2). We observe that the Freundlich model ($R^2 = 0.993$) represented better the adsorption isotherms of MO on ($BiMgFeO_4$) nanoferrite than the Langmuir model ($R^2 = 0.988$). This suggests that the sites were heterogeneous, with the possibility of more than one adsorption monolayer on the ferrite surface.

On the other hand, when $BiMgFeO_4$/Bentonite was the adsorbent, we observe that the correlation coefficients were close to unit ($R^2 = 0.993$) in the Langmuir model and ($R^2 = 0.985$) for the Freundlich model. We conclude that the Langmuir model was the most consistent with the experimental data. The n value of the Freundlich model calculated for the two adsorbents was always between zero and one. These results verify that the adsorption process of MO on the composite was favorable.

3.6.8 Isosteric Heat of Adsorption

The isosteric heat of adsorption Q_{st} (kJ.mol^{-1}) is the amount of heat developed during the adsorption of one mole of MO dye by one gram of adsorbent. It was determined at a constant amount of adsorbate adsorbed (Qe = 30, 32, 34, 36, 38 mg. g^{-1}) and was calculated using the Clausius–Clapeyron equation given by the following relation where $\Delta H_{ads} = -Q_{st}$

$$\frac{\mathrm{d(lnCe)}}{\mathrm{dt}} = -\frac{\Delta \mathrm{H_{ads}}}{\mathrm{RT^2}}$$

$$\mathrm{Ln}(Ce) = \frac{\Delta H_{ads}}{RT} + constant$$

For this purpose, the equilibrium concentration (Ce) at a constant amount of methyl orange adsorbed was obtained from the isotherm data at different temperatures. Ln Ce versus 1/T plots were found to be linear (Fig. 15), and the slopes of the plots were used to calculate the values of ΔH_{ads} for different amounts of adsorbate on the two adsorbents separately.

The R^2 values of the isosteres and the corresponding ΔH_{ads} values for the adsorption of MO on the two prepared adsorbents are listed in the following table (Table 5) at different values of the amount of methyl orange adsorbed at equilibrium Qe (mg. g^{-1}).

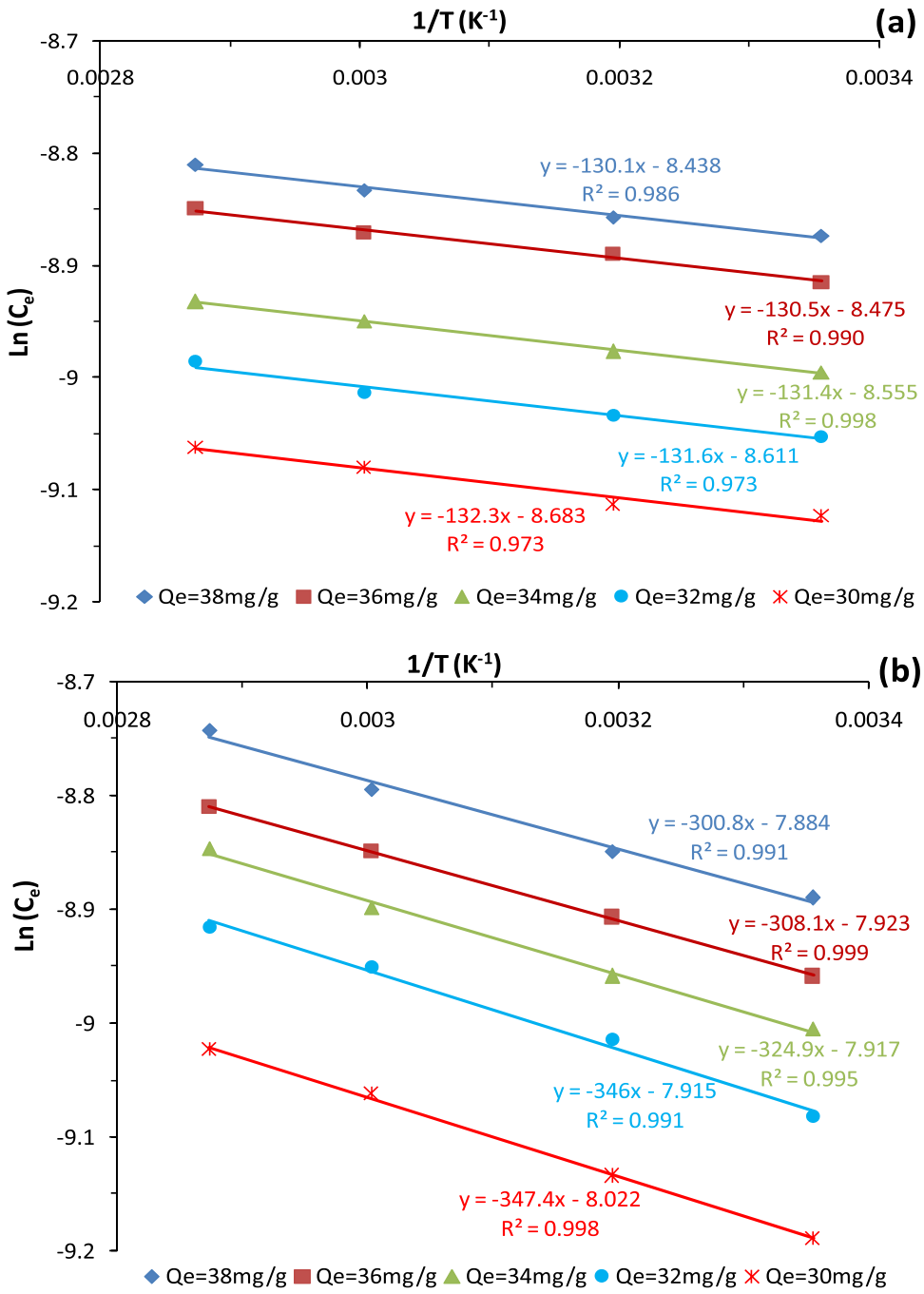

Fig. 15 Plots of Ln Ce versus 1/T for adsorption of MO onto $BiMgFeO_4$ nanoferrite (**a**), and $BiMgFeO_4$/Bentonite composite (**b**)

Table 5 Isosteric heat of adsorption of MO onto $BiMgFeO_4$ nanoferrite and on $BiMgFeO_4$/Bentonite composite

Adsorbent	$BiMgFeO_4$		$BiMgFeO_4$/Bentonite	
Q_e (mg.g^{-1})	ΔH_{ads} (kJ. Mol^{-1})	R^2	ΔH_{ads} (kJ. Mol^{-1})	R^2
30	− 1.100	0.973	− 2.88	0.998
32	− 1.094	0.973	− 2.87	0.991
34	− 1.092	0.998	− 2.70	0.995
36	− 1.085	0.990	− 2.56	0.999
38	− 1.081	0.986	− 2.50	0.991

Figure 15a displays the variation of Ln Ce versus 1/T for different amounts of $BiMgFeO_4$ nanoferrite, and Fig. 15b displays the variation of Ln Ce versus 1/T for different amounts of adsorbate for adsorption of MO onto $BiMgFeO_4$/Bentonite composite.

The negative values of isosteric heat of adsorption confirm the exothermic adsorption process. Moreover, the heat of physical adsorption, which involves only relatively weak intermolecular forces such as van der Waals and electrostatic interactions, is typically lower than that of chemisorption, which involves the formation of a chemical bond between

adsorbate molecules and the adsorbent's surface. The upper limit for Qst physical adsorption, known as physisorption, should be 80 kJ.mol^{-1} for adsorption on adsorbents, while the highest limit for chemical adsorption, called chemisorption, which is characterized by covalent bonding, should be between 80 and 400 kJ mol^{-1} [79]. In the present work, the values of isosteric heat of methyl orange adsorption ranged between 1.081 and 1.1 kJ.mol^{-1} for the prepared ferrite, and between 2.5 and 2.88 kJ.mol^{-1} for its composite.

The preceding results suggest that the interaction between the surface of both (Mg-doped bismuth ferrite) and the composite (Mg-doped bismuth ferrite-bentonite) and MO dye molecules was a physisorption, involving weak van der Waals and electrostatic interactions.

3.6.9 Comparison with Other Adsorbents

A comparison of the maximum adsorption capacity (q_{max} value) for MO on magnesium doped magnetic nanoferrite and its bentonite-based composite, with those of other adsorbents published by other studies, was demonstrated (Table 6). Magnesium doped magnetic nanoferrite and its bentonite-based composite were relevant and promising for the removal of MO from aqueous solutions because they had a relatively higher adsorption capacity than many other magnetic adsorbents.

4 Conclusion

This study demonstrated the effectiveness of nano-adsorbent based on magnetic ferrite (Mg-doped bismuth ferrite) and its clay-based Mg-doped bismuth ferrite-bentonite in removing methyl orange dye in aqueous medium. Adsorbents were produced using a self-combustion process with glycine as the fuel. The effect of operating-condition factors such as contact time, adsorbent dose, pH, and temperature, was investigated.

Increasing the adsorbent mass generated an increase of the adsorption capacity of the anionic dye for both adsorbents. However, the percentage of the solution dye decolorization was higher with the ($BiMgFeO_4$/Bentonite) composite. It reached ~ 91.3% for 150 mg of adsorbent in 100 mL of solution, while it is ~ 71.3% for ($BiMgFeO_4$) nanoferrite as adsorbent with the same dose. Moreover, acidic pH was the optimal medium to have better adsorption of the MO anionic dye on both adsorbents.

The equilibrium was attained after 300 min for the Mg-doped bismuth ferrite, and after 180 min for the $BiMgFeO_4$/Bentonite composite, according to the kinetic analysis. Furthermore, the adsorption process for both the produced ferrite and its composite could be explained by pseudo-second order kinetics.

The plot of the adsorption isotherms confirms that the adsorption process of methyl orange on both the ferrite and its composite was favorable. The Freundlich model perfectly represented adsorption of MO dye to the prepared Mg-doped bismuth ferrite with a maximum adsorption capacity of 181.8 mg. g^{-1} at 298 K. This suggests that the sites were heterogeneous, with the possibility of more than one adsorption monolayer on the ferrite surface. While, Langmuir model seemed to be the most suitable model for the absorption of methyl orange to the Mg-doped bismuth-bentonite composite, with a maximum adsorption capacity of 188.8 mg. g^{-1} at 298 K. The n value of the Freundlich model, which is related to the adsorption intensity and surface heterogeneity, gave evidence that the adsorption is favorable for both adsorbents. The coefficient n was greater in the case of the composite than in the case of the ferrite, revealing that the composite had higher adsorption of MO dye.

Table 6 Comparison of the Adsorption Capacity for methyl orange on magnesium doped magnetic nanoferrite and its bentonite-based composite with other adsorbents

Adsorbent	Adsorption capacity (mg. g^{-1})	Experimental conditions	References
Modified fly ash with $Ca(OH)_2$/Na_2FeO_4	23.8	25 °C, pH = 10	[80]
Fe_2O_3-biochar nanocomposite	20.53	25 °C, pH = 8	[81]
β-cyclodextrin/Fe_3O_4/polyvinylpyrrolidone	47.62	25 °C, pH = 7	[82]
Magnetic lignin-based carbon nanoparticles	113	20 °C, pH = 5	[83]
Magnetic Lignin-based	85	25 °C, pH = 5	[84]
Fe_3O_4/Al_2O_3/chitosan composite	416	25 C, pH = 6	[85]
γ-Fe_2O_3/2C nanocomposite	72.7	25 °C, pH = 4.8	[86]
Magnetic Activated Carbons	189.2	35 °C, pH = 2.8	[87]
Maghemite/chitosan nanocomposite films	29.41	57 °C, pH = 3	[88]
Mg-doped bismuth ferrite	181.8	25 °C, pH = 6	This study
Mg-doped bismuth ferrite/bentonite	188.8	25 °C, pH = 6	This study

It was also established that the composite has a mesoporous structure, which was favorable for the removal of the MO anionic dye.

The thermodynamic parameters indicated that the adsorption of methyl orange was an exothermic process with a random distribution of MO dye molecules over the adsorbent surface.

The determination of isosteric heat of adsorption for both prepared adsorbents suggested that it is indeed a physisorption characterized by weak intermolecular forces between adsorbate and the adsorbent surface.

Supplementary Information The online version contains supplementary material available at https://doi.org/10.1007/s42250-022-00343-2.

Declarations

Conflict of interest The authors declare no conflict of interest.

References

1. Guerra E, Llompart M, Garcia-Jares C (2018) Analysis of dyes in cosmetics: challenges and recent developments. Cosmetics 5(3):47
2. Masoumeh G, Najmeh Z, Fatemeh K, Ceren K, Marzieh A, Yasser V (2022) Recent advances in Ponceau dyes monitoring as food colorant substances by electrochemical sensors and developed procedures for their removal from real samples, Food Chem Toxicol 161:112830
3. Ninad O, Mohan S (2022) Development of nanoporous textile sludge-based adsorbent for the dye removal from industrial textile effluent. J Hazardous Materials 422:126864
4. Angelika T , Kamila M, Andrzej P (2020) Synthetic organic dyes as contaminants of the aquatic environment and their implications for ecosystems: a reviewer. Sci Total Environ 717:137222
5. Tiwari A, Joshi M, Salvi N, Gupta D, Gandhi S, Rajpoot K, KumarTekade R (2022) Chapter 21 - Toxicity of pharmaceutical azo dyes, Pharmacokinetics and Toxicokinetic Considerations. Ad Pharmaceut Product Dev Res 2: 569–603
6. Zhang W, Yan H, Li H, Jiang Z, Dong L, Kan X (2011) Removal of dyes from aqueous solutions by Straw-based adsorbents: batch and column studies. Chem Eng J 168:1120–1127
7. Al-Tohamy R, Alia SS, Kamal FL, Okashad M, Mahmoud YA-G, Elsamahy T, Jiao H, Fu Y, Sun J (2022) A critical review on the treatment of dye containing wastewater: Ecotoxicological and health concerns of textile dyes and possible remediation approaches for environmental safety. Ecotoxicol Environ Saf 231: 113160
8. Bee Ã, Rocher V, Siaugue J (2008) Removal of organic dyes by magnetic alginate beads, 42:1290–1298
9. Bing K, Vakili M, Amini B, Eong P, Zuhairi A, Salamatinia B (2015) Adsorption of dyes by nanomaterials: recent developments and adsorption mechanisms. Sep Purif Technol 150:229–242
10. Removal C, Textile F (1996) Color removal from textile 34: 9–16
11. Panchamoorthy K, Murugesan S, Abraham J, Muthukumar K (2009) Bioresource Technolog Bacillus sp. mutant for improved biodegradation of Congo red : random mutagenesis approach. Bioresour Technol 100:6295–6300
12. Ciardelli G, Corsi L, Marcucci M (2000) Membrane separation for wastewater reuse in the textile industry 31:189–197
13. Mantzavinos D, Psillakis E (2004) Enhancement of biodegradability of industrial wastewaters by chemical oxidation pre-treatment 454:431–454
14. Dhahri R, Bouzidi A, Moussaoui Y (2021) Activated carbon from prickly pear seeds: optimization of preparation conditions and cadmium removal using experimental design approach, in: 2021: pp 1457–1461
15. Gayathiri M, Pulingam T, Lee KT, Sudesh K (2022) Activated carbon from biomass waste precursors: Factors affecting production and adsorption mechanism. Chemosphere 294:133764.
16. Huang Z, Gao P, Zheng H, Liu X, Wen J (2019) Magnetic enrichment behavior of monodispersed MFe2O4 nanoferrites (M = Mg, Ca, Ni Co, and Cu). Ceram Int 45:15980–15989
17. Ai L, Zhou Y, Jiang J (2019) Removal of methylene blue from aqueous solution by montmorillonite/$CoFe_2O_4$ composite with magnetic separation performance. Desalination 266(1–3):72–77
18. Atia AA, Donia AM, Al-Amrani WA (2009) Adsorption/desorption behavior of acid orange 10 on magnetic silica modified with amine groups. Chem Eng J 150(1):55–62
19. Qadri S, Ganoe A, Haik Y (2009) Removal and recovery of acridine orange from solutions by use of magnetic nanoparticles. J Hazard Mater 169(1–3):318–323
20. Chand P, Vaish S, Kumar P (2017) Structural, optical and dielectric properties of transition metal (MFe_2O_4; M = Co, Ni and Zn) Nanoferrites Structural, optical and dielectric properties of transition metal (MFe_2O_4; M = Co, Ni and Zn) nanoferrites. Phys B Phys Condens Matter 524:53–63
21. Huang Y, Zhang B, Liu B, Han G, Du Y, Su S (2022) Adsorption behaviors of strategic W/Mo/Re from wastewaters by novel magnetic ferrite nanoparticles: adsorption mechanism underlying selective separation. J Hazardous Materials 424(Part D): 127675
22. Pan X, Sun A, Han Y, Zhang W, Zhao X (2019) Structural and magnetic properties of Bi^{3+} ion doped Ni – Cu – Co nano ferrites prepared by sol – gel auto combustion method. J Mater Sci Mater Electron
23. Pathania A, Rana K, Bhalla N, Thakur P (2017) Mossbauer, spectroscopic studies of tungsten doped Raman and Mo Ni – Zn nano ferrite. J Mater Sci Mater Electron 28:679–685
24. Gul IH, Sutka A, Lagzdina S (2017) Structural and dielectric properties of bismuth doped cobalt nano ferrites prepared by Sol-Gel auto combustion method structural and dielectric properties of bismuth doped cobalt nano ferrites prepared by Sol-Gel auto combustion method, 0–11
25. Mansour SF, Al-wa R, Abdo MA (2020) Zn-Mg-La nanoferrites for storage and high frequency devices with augmenting the photocatalytic performance, 826
26. Taneja S, Chahar D, Thakur P, Thakur A (2020) Remarkable resistivity and improved dielectric properties of Co–Zn nanoferrites for high frequency applications. J Alloy Compd 843:30155681
27. Shakil M, nayat U, .Khalid NR, Tanveer M, Gillani SSA, Tariq NH, Shah A, Mahmood A, Dahshan A (2022) Enhanced structural, optical, and photocatalytic activities of Cd–Co-doped Zn ferrites for degrading methyl orange dye under irradiation by visible light. J Phys Chem Solids 161:110419
28. Camacho-Gonz A, Garrido- A, Ramírez-Ayala MF, Esperanza L (2019) Synthesis and characterization of magnetic zinc-copper ferrites: antibacterial activity, photodegradation study, and heavy metals removal evaluation, 236
29. Pre-proofs J (2020) Significantly improved solar photodegradation of water pollutant by new plate-like bismuth ferrite nanoparticles tuned by gelatin, Elsevier B.V.
30. Tatarchuk T, Myslin M, Lapchuk I, Shyichuk A, Murthy AP, Gargula R, Kurzydło P, Bogacz BF, Pędziwiatr AT (2021) Magnesium-zinc ferrites as magnetic adsorbents for Cr(VI) and Ni(II) ions removal: Cation distribution and anti-structure modeling. Chemosphere 270:129–414

31. S. Naz, T. Rasheed, S. Tayyab, R. Naqvi, D. Hussain, B. Fatima, M. Najam, S.Majeed, S. Shafi, K. Rizwan, M. Ibrahim, Physica B : Physics of Condensed Matter, Polyvinylpropyllidone decorated manganese ferrite based cues for the efficient removal of heavy metals ions from wastewater, Phys. B Phys. Condens. Matter. 599 412559, (2020).
32. Caille`re S, Henin S, Rautureau M (1982) Minéralogie des argiles : Structure et propriétés Physico chimiques Tome II, Edition Masson, Paris
33. Bouchet A, Meunier A, Sardini P (2000) Minéraux argileux, Edition Eyrolles
34. Elkhider KHA, Ihsanullah I, Zubair M et al (2020) Synthesis, characterization and dye adsorption performance of a magnetic bentonite-CoNiAl composite decorated Bentonite-CoNiAl Magnetic Composite. Arab J Sci Eng 45:7397–7408
35. Sanad MMS, Farahat MM, Abdel Khalek MA (2021) One-step processing of low-cost and superb natural magnetic adsorbent: kinetics and thermodynamics investigation for dye removal from textile wastewater. Adv Powder Technol (32)5:1537–1583
36. Zhang H, Liang X, Yang C, Niu C, Wang J, Su X (2016) Nano γ-Fe_2O_3 /bentonite magnetic composites: synthesis, characterization, and application as adsorbents. J Alloys Compounds 688:1019–1027
37. An S, Liu X, Yang L, Zhang L (2015) Enhancement removal of crystal violet dye using magnetic calcium ferrite nanoparticle: study in single- and binary-solute systems. Chem Eng Res Des 94:726–735
38. Wu KH, Ting TH, Li MC, Ho WD (2006) Sol-gel auto-combustion synthesis of SiO_2 -doped NiZn ferrite by using various fuels 298:25–32
39. Nasri H, Kermani S, Ammar Abbassi M, Omri A (2020) Characterization of Sand From Jebel Ad-Darin Sened (Gafsa-Tunisia), September
40. Bhasker U, Yelasani V, . Ramana V, Musugu R (2015) Journal of Magnetism and Magnetic Materials Structural , electrical and magnetic characteristics of nickel substituted cobalt ferrite nano particles, synthesized by self combustion method. J Magn Magn Mater 374
41. Rehman AU, Morley NA, Amin N, Arshad MI, un Nabi MA, Mahmood K, Ali A, Aslam A, Bibi A, Iqbal MZ, Iqbal F, Bano N, Alzaid M (2020) Controllable synthesis of La3+ doped Zn0.5Co0.25Cu0.25Fe2−xLaxO4 (x = 0.0, 0.0125, 0.025, 0.0375, 0.05) nano-ferrites by sol-gel auto-combustion route. Ceram Int 46:29297–29308
42. Newcombe G, Hayes R, Drikas M (1993) Granular activated carbon: Importance of surface proprieties in the adsorption of naturally occurring organics. Colloids Surfaces A 65–71
43. Guo X, Wang J (2019) Comparison of linearization methods for modeling the Langmuir adsorption isotherm. J Mol Liq 296:111850
44. Freundlich H (1899) Über die Adsorption in Lösungen 1: 1334
45. Shaikh AM, Jadhav SA, Watawe SC, Chougule BK (2000) Infrared spectral studies of Zn-substituted Li – Mg ferrites 192–196
46. Abbas M, Rao BP, Naga SM, Takahashi M, Kim C (2013) Author's accepted manuscript. Ceram Int
47. Dhanya SR, Nair SG, Satapathy J, Pavan Kumar N (2019) Structural and spectroscopic characterization of bismuth ferrite. AIP Conf Proc 2166:020017
48. Peñalva1 J, Lazo A (2018) Synthesis of Bismuth Ferrite BiFeO3 by solution combustion Method IOP Conf. Series. J Phys 1143:012025
49. Peñalva J, Lazo A (2018) Journal of Physics: Conference Synthesis of Bismuth Ferrite BiFeO3 by solution combustion method, Series
50. Yue Z, Guo W, Zhou J, Gui Z, Li L (2004) Synthesis of nanocrystilline ferrites by sol–gel combustion process: the influence of pH value of solution. J Mag Mag Materials 216–223
51. Yen-Chun La, Yen-Pei Fb (2010) Magnetic and catalytic properties of copper ferritenanopowders prepared by a microwave-induced combustion process. Ceramics Int 36:1597–1601
52. Thommes M, Cychosz KA (2014) Physical adsorption characterization of nanoporous materials: progress and challenges. Adsorption 20:233–250
53. Sing K (2001) Review about The use of nitrogen adsorption for the characterization of porous materials. Colloids Surf, A 187–188:3–9
54. Sing KSW, Everett DH, Haul RAW, Moscou L, Pierotti RA, Rouquerol J, Siemieniewska T (1985) Reporting physisorption data for gas/solid systems with with special reference to the determination of surface area and porosity. Pure App Chem 57:603–619
55. Gelb LD, Gubbins KE (1999) Langmuir 15(2):305–308
56. Mihayo D, Rao Vegi M, Ali Hamad Vuai S (2021) Defluoridation of aqueous solution using thermally activated biosorbents prepared from adansonia digitata fruit pericarp. Adsorption Sci 2021, Article ID 5574900, 16
57. Stoeckli F, Moreno Ramon MV, Moreno-Castilla C, Carrasco Castilla C (1999) Carrasco Marin. Carbon 37:1215–1221
58. Shao Y, Wang X, Kang Y et al. (2014) Application of Mn/ MCM-41 as an adsorbent to remove methyl blue from aqueous solution. J Colloid Interface Sci 429:25–33
59. Hameed BH (2010) Evaluation of papaya seed as a novel non-conventional low-cost adsorbent for removal of methylene blue. J Hazard Mater 162:939–994
60. Patil AK, Shrivastava VS (2010) Alternanthera bettzichiana plant powder as low cost Adsorbent for removel of congo red from aqueous solution. Int J Chemtech Res 2:842–850
61. Centre R (2013) Adsorption of Lead from Aqueous Solution by Manganese Ferrite Nanoparticles 25:9920–9926
62. Dincer AR, Guner Y, Karakaya N (2006) Coal-based botton ash (CBBA) waste material as adsorbent for removal of textile dyestuffs from aqueous solution. Colloid Interface Sci 293:303–311
63. Mall ID, Srivastva VC, Agarwal NK, Mishra IM (2005) Removal of Congo red from aqueous solution by baggase fly ash and activated carbon: kinetic study and equilibrium isotherm analyses. Chemosphere 61:492–501
64. Dogan M, Alkan M, Demirabas O, Ozedemie Y, Ozemetin C (2006) Adsorption kinetics of maxilon blue GRL onto sepiolite from aqueous solution. Chem Eng J 124:89–101
65. Lagergren S (1898) Zur theorie der sogenannten adsorption geloester stoffe. Kungliga Svenska Vetenskapsakad. Handlingar 24:1–39
66. Ho YS, Mckay G (1999) Pseudo-second order model for sorption processes 34:451–465
67. Luo Z, Gao M, Yang S, Yang Q (2015) Colloids and surfaces a: physicochemical and engineering aspects adsorption of phenols on reduced-charge montmorillonites modified by bispyridinium dibromides: mechanism, kinetics and thermodynamics studies. Colloids Surfaces A Physicochem Eng Asp 482:222–230
68. Langmuir I (1918) The adsorption of gases on plane surfaces of glass, mica and platinum. J Am Chem Soc 40(9):1361–1403
69. Araissi M, Ayed I, Elaloui E, Moussaoui Y (2016) Removal of barium and strontium from aqueous solution using zeolite 4A., Water Sci Technol. 73:16–36
70. Qing-Song L, Tong Z, Peng W, Ji-Ping J, Nan L (2010) Adsorption isotherm, kinetic and mechanism studies of some substituted phenols on activated carbon fibers. Chem Eng J 157:348–356
71. Liu QS, Zheng T,Wang P, Jiang JP, Li N (2010) Adsorption isotherm, kinetic and mechanism studies of some substituted phenols on activated carbon fibers. Chem Eng J 157:348–356

72. Foo KY, Hameed BH (2010) Insights into the modeling of adsorption isotherm systems. Chem Eng J 156:2–10
73. Shen D, Fan J, Zhou W, Gao B, Yue Q, Kang Q (2009) Adsorption kinetics and isotherm of anionic dyes onto organo-bentonite from single and multisolute systems. J Hazard Mater 172:99–107
74. Islam MT, Aimone F, Ferri A, Rovero G (2015) Use of N-methylformanilide as swelling agent for meta-aramid fibers dyeing: kinetics and equilibrium adsorption of Basic Blue 41. Dyes Pigm 113:554–561
75. Dawood S, Sen TK (2012) Removal of anionic dye Congo red from aqueous solution by raw pine and acid-treated pine cone powder as adsorbent: equilibrium, thermodynamic, kinetics, mechanism and process design. Water Res 46:1933–1946
76. Errais E, Duplay J, Darragi F, M'Rabet I, Amélie Aubert A, Huber F, Morvan G (2011) Efficient anionic dye adsorption on natural untreated clay: kinetic study and thermodynamic parameters. Desalination 275:74–81
77. Akbal F (2005) Sorption of phenol and 4-chlorophenol onto pumice treated with cationic surfactant. J Environ Manage 74:239–244
78. Rauf MA, Bukallah SB, Hamour FA, Nasir AS (2008) Adsorption of dyes from aqueous solutions onto sand and their kinetic behaviour. Chem Eng J 137:238–243
79. Demirak A, Dalman O, Tilkan E, Dilek Yildiz D, Yavuz E, Gökçe C (2011) Biosorption of 2,4 dichlorophenol (2,4-DCP) onto Posidonia oceanica (L.) seagrass in a batch system: Equilibrium and kinetic modelling. Microchem J 99:97-102
80. Gao M, Ma Q, Lin Q, Chang J, Bao W, Ma H (2015) Combined modification of fly ash with Ca(OH)2 /Na2 FeO4 and its adsorption of Methyl orange. Appl Surf Sci 359:323–330
81. Chaukura N, Murimba EC, Gwenzi W (2016) Synthesis, characterisation and methyl orange adsorption capacity of ferric oxide–biochar nano-composites derived from pulp and paper sludge. Appl Water Sci 7:2175–2186
82. Si Q, Wen Q, Yang Q, Song Y, Li Y (2017) Preparation of β-cyclodextrin /Fe_3O_4/polyvinylpyrrolidone composite magnetic microspheres for the adsorption of methyl orange. Chem Res Chinese Univ 33:1012–1016
83. Ma Y, Zheng D, Mo Z, Dong R, Qiu X (2018) Magnetic lignin-based carbon nanoparticles and the adsorption for removal of methyl orange. Colloids Surfaces A
84. Cao C, Shao L, Lucia LA, Liu Y (2021) Fabrication of magnetic lignin-based adsorbent for removal of methyl orange dye from aqueous solution. BioResources 16(3):5436–5449
85. Tanhaei B, Ayati A, Lahtinen M, Sillanpää M (2015) Preparation and characterization of a novel chitosan/Al_2O_3/magnetite nanoparticles composite adsorbent for kinetic, thermodynamic and isotherm studies of Methyl Orange adsorption. Chem Eng J 259:1–10
86. Istratie R, Stoia M, Păcurariu C, Locovei C (2019) Single and simultaneous adsorption of methyl orange and phenol onto magnetic iron oxide/carbon nanocomposites. Arabian J Chem 12(8):3704–3722
87. Cordova Estrada AK, Cordova Lozano F, Lara Díaz RA (2021) Thermodynamics and kinetic studies for the adsorption process of methyl orange by magnetic activated carbons. Air Soil Water Res 14:1–11
88. Jiang R, Fu Y-Q, Zhu H-Y, Yao J, Xiao L (2012) Removal of methyl orange from aqueous solutions by magnetic maghemite/chitosan nanocomposite films: adsorption kinetics and equilibrium. J Appl Polym Sci 125(S2):E540–E549